ELSEVIER

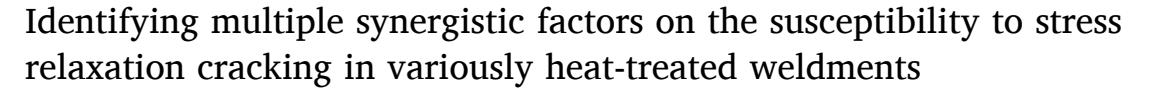
Contents lists available at ScienceDirect

Mechanics of Materials

journal homepage: www.elsevier.com/locate/mechmat



Research paper



Yi Yang ^{a, b}, Dong Han ^a, Wei Zhang ^b, Yanfei Gao ^{a, *}, Jorge Penso ^{c, **}, Zhili Feng ^{b, ***}

- ^a Department of Materials Science and Engineering, University of Tennessee, Knoxville, TN, 37996, USA
- ^b Material Science and Technology Division, Oak Ridge National Laboratory, Oak Ridge, TN, 37831, USA
- ^c Shell Global Solution (US) Inc, TX, 77082, USA

ARTICLE INFO

Keywords:
347H stainless steel weldments
Residual stress
Intergranular grain-boundary cavity failure
Stress relaxation cracking

ABSTRACT

The 347H austenitic stainless steel has been widely used for pressure vessels and pipeline (PVP) applications due to its excellent creep and corrosion resistance, which fit ideally to the harsh conditions in petrochemical industries, fossil fuel or nuclear power plants, and modern energy storages. However, a failure mode has been commonly observed with cracks emerging at the heat affected zone (HAZ) of weldments during post-weld heat treatment (PWHT) or under intermediate to high temperature service conditions. This phenomenon is termed as Stress Relaxation Cracking (SRC) since the purpose of PWHT is to relieve the welding-induced residual stress fields, or as Stress Age Cracking (SAC) if failure happens during service. A leading literature explanation of this failure suggests that the residual stress relaxation and the precipitation dissolution and/or re-precipitation occur in the same temperature range, which can lead to locally high strains and thus to crack at the grain boundaries. Since in situ spatial measurements of residual stress fields, microstructural evolution, and failure processes are nearly infeasible, this work recourses to a micromechanical finite element framework that models the high temperature failure as the nucleation and growth of grain boundary cavities, whereas various parameters such as thermomechanical loading history and its evolution, the competition of grain-interior dislocation creep and grain-boundary diffusion in failure lifetime, and microstructural heterogeneities (such as the precipitate free zone near grain boundaries) can be quantitatively incorporated. It can be concluded from these microstructureexplicit simulations that an accurate knowledge of residual stress evolution and a carefully calibrated set of material constitutive parameters are the essential prerequisites for lifetime predictions. The understanding of individual governing factors also leads to a mechanistic interpretation of the observed SRC susceptibility Ccurves. These results suggest that the criticality of residual stress evolution, but not the precipitation-induced local strains, be the leading factor for SRC.

1. Introduction

Material selection and structural integrity studies in pressure vessels and pipeline (PVP) have been extensively studied for traditional petrochemical and power-generation industries. Challenges arise with modern energy storage and transportation that connect clean energy production to the power grid, and also with more pressing needs in revisiting and redesigning structural components due to the aging infrastructure in the US. Welding is the primary joining method used in PVPs due to its operational convenience and capability to maintain the

thermal-mechanical properties of the materials after joining compare to other methods (Bauer and Lessmann, 1976). Despite the adoption of optimal welding techniques, unexpected failures still occur during service, with the majority of failure cases in pipeline systems occur at weldments. Of the particular importance is the stress relaxation cracking (SRC) or called strain aging cracking (SAC), where cracks emerge at variously heat-treated weldments (Kromm et al., 2020; Chang et al., 2011; Nawrocki et al., 1999, 2003; Sarich et al., 2022). The generation of the residual stress is the result of the local melting process, the rapid heating and cooling which cause the thermal expansion and contraction

E-mail addresses: ygao7@utk.edu (Y. Gao), Jorge.Penso@shell.com (J. Penso), fengz@ornl.gov (Z. Feng).

https://doi.org/10.1016/j.mechmat.2024.105013

^{*} Corresponding author.

^{**} Corresponding author.

^{***} Corresponding author.

in the fusion zone (FZ) and heat affected zone (HAZ). A subsequent reheating could be the post-welding heat treatment (PWHT) that aims to relieve the residual stress (thus leading to the calling of SRC if crack occurs in this stage), or the service condition at intermediate or high temperatures (thus leading to the name of SAC). We will focus on a generalized thermal history and thus do not differentiate these two terms in this work. The highest susceptibility to such a failure mode occurs when a high accumulation of residual stress, thermomechanical property and microstructural gradients, and their evolutions are all present. These multiple factors contribute synergistically to the eventual failure mechanism as governed by the operating conditions and microstructural information.

The SRC susceptibility has a close correlation with the pipe material and its operating conditions. The typically employed materials include X52 steel, Nippon X65, TMCP X60-1/2, P91, 304, 316L, and 347H due to their ability to resist corrosion and creep (Mahajanam and Joosten, 2011; Wu et al., 2020; Zhang et al., 2020). As these pipeline systems are often subjected to mid-to high-temperature and corrosive working conditions, the service pipe components must perform well under such a critical environment while also being cost-effective. Therefore, stainless steel, instead of Ni-based superalloys, is often the preferred choice due to its comparable mechanical properties and lower cost. In this study, we focus on the thermomechanical impact on the failure process of 347H austenitic stainless steel, which is known to contain segregation-prone elements such as B, C, Nb, Si, and Mo. Carbide precipitates provide the needed creep resistance, but they are believed to contribute to SRC since their dissolution and re-precipitation take place at the same temperature range as the heat treatment and/or service conditions (Siefert et al., 2016). A critical task in this area is to develop a method that can simulate the entire failure process and provide a reasonable estimation of the failure lifetime under all these synergistic factors. Unfortunately, this has not been achieved due to several key challenges as elaborated

The first challenge lies on the determination of residual stress evolution with respect to the thermal history. Needleless to say, residual stress measurements of welded structures have been routinely done at ambient conditions, but a nondestructive real-time measurement at high temperature still remains elusive. Commonly used nondestructive methods include Barkhausen noise method, X-ray diffraction method, neutron diffraction method and ultrasonic method, semi-destructive methods include hole-drilling technique, ring-core method and deephole method, and the destructive methods include sectioning technique and contour method (Rossini et al., 2012). However, using different methods easily lead to contrasting residual stress levels and sometimes the signs can even be flipped. Such challenges have prevented us from developing an optimal temperature history that can prevent SRC. For example, a higher PWHT temperature can result in a more uniform and lower residual stress field which can prolong the lifetime of the pipeline system (Dong et al., 2014). PWHT is typically applied after the welding process to reduce residual stress level. The percentage of residual stress reduction depends on the PWHT temperature, with higher temperatures leading to more rapid relaxation of residual stress. While this can be beneficial for reducing residual stress, it can also increase the SRC susceptibility due to some undesirable microstructural changes. A dissolution of precipitates leads to a precipitate-free zone (PFZ) near grain boundaries, and the resulting strain redistribution and accumulation at these sites is believed to be the culprit for SRC to take place (Siefert et al., 2016). However, there is no detailed stress mapping to validate this hypothetical process.

The second challenge in this study is concerned with the controlling failure mechanism. Previous research (Nawrocki et al., 1999; Shin and McMahon, 1984) indicates that creep rupture, or a coupled mechanism including diffusion and creep failure are typical modes of failure control. The formation of cavities at grain boundaries and their accumulation under thermal-mechanical field are the root cause, with precipitation evolution playing a key role in cavity coalescence, crack initiation and

propagation, especially in the case of precipitation preferentially formed at grain boundaries. The above behaviors can be explained through an failure mechanism or their Diffusion-controlled failure is more likely to occur at high-temperature service conditions. For the service temperature range considered in this study, failure is first controlled by dislocation creep in grain interior due to the high stress level, and then changed to diffusion control as the applied stress (here residual stress) decreases and the service temperature increases. The broad range of thermal treatment temperatures from mid-to high-temperature adds further complexity to determining the controlling mechanism of failure. Previous research has used simulations to predict lifetime. For example, Hayhurst et al. (2005) used a continuous damage method to predict the lifetime of high-temperature, low-alloy ferritic steel weldments. This model was successful in identifying the failure location, although the prediction error was noticeable when comparing 2D to 3D results, and even more obvious to experimental data. Gaffard et al. (2005) focused on revealing the relationship between microstructure state and low creep strength in weldments, and correlated experiments and model were developed. However, the limitations of the sample shape and the ability to extrapolate to other conditions must be noted. In order to address the failure process more precisely, the simulation model in this study needs to be microstructure-explicit and based on grain boundary cavities, with certain constitutive laws governing cavity nucleation and growth and with direct connections to grain boundary diffusion, viscous grain boundary sliding, and other mechanisms.

Yet another crucial challenge is on the role played by the microstructural evolution. The intricate relationship between precipitate generation and annihilation, as well as changes in thermal-mechanical properties, can affect the failure process. For example, the working environment significantly affects the thermal-mechanical properties variation of 347H austenitic stainless steel, which is a high alloy-type precipitation strengthening material. Examples of such variation include an increase in creep rate, a decrease in yield strength, and the gradual evolution of precipitation over time. Several types of precipitates exist in 347H SS at different stages of service, including NbC, $Cr_{23}C_6$, Fe-rich α , Cr-rich α' , sigma phase, G-phase, Z-phase (NbCrN), and Laves phase. The appearance sequence of different precipitates determines the level of crack initiation and propagation. For example, during the stabilizing annealing stage, NbC has a high correlation with reducing the susceptibility to intergranular cracking of the material. During the welding and PWHT stage, a synergistic process occurs wherein Cr₂₃C₆ formation in the HAZ takes place, along with carbon redistribution. As transferring to the service stage with in temperature range of approximately 400 $^{\circ}$ C, the formation of Fe-rich α , Cr-rich α' , and G-phase occurs due to ferrite spinodal decomposition (Wu et al., 2020). The effect of each phase is different; for example, the formation of Cr₂₃C₆ and sigma phase has no contribution to strengthening because they accumulate along the grain boundaries, providing nucleation sites for cavities, serving as a driving force for crack initiation, and contributing to the carbon-free process (Kim et al., 2007; Pulliam, 1959). The effects of other types of precipitation have not been clearly defined. The precipitation size and distribution significantly affect microstructure evolution, and differences in grain size, precipitation fraction, and precipitation type variation dictate the degradation of mechanical properties in various locations.

Since the failure time can reach months or years in actual working conditions, accelerated laboratory experiments have to be employed to mimic and reproduce SRC. As shown by the compiled data in Fig. 1, a 100% or 90% yield stress level is usually used as the applied stress level to shorten the lifetime, although the temperature range follows the PWHT or service conditions. Even though these experiments and actual cases show the same intergranular cavities after failure, the higher stress level in such accelerated tests than the residual stress level may lead to different mechanisms that govern the cavity growth process. Despite this potential risk, the testing data presented in Fig. 1 demonstrate a C-type

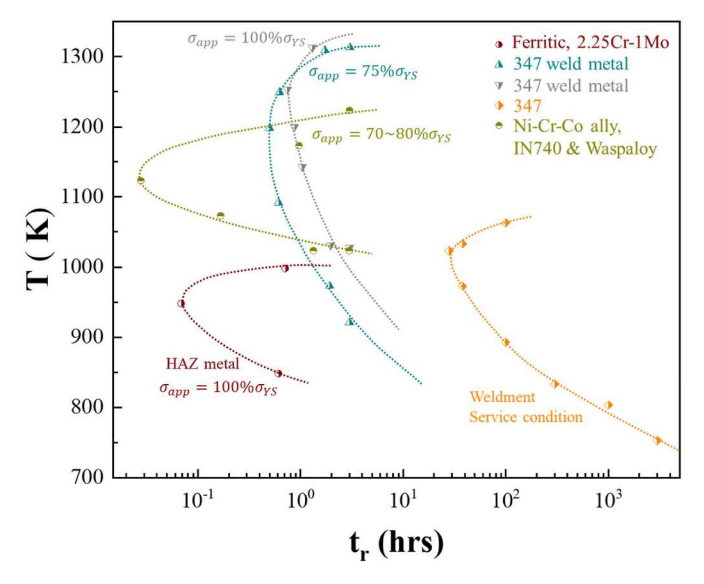


Fig. 1. Stress-relaxation-cracking (SRC) susceptibility curves showing the temperature-lifetime relationship for various materials and their weldments, whereas some are subjected additional applied load and some are purely driven by welding-induced residual stress. Due to their shape, these curves are also called SRC C-curves.

behavior, that is, there exists a lowest lifetime if the reheating-and-hold temperature is at an intermediate level. These C-curves are more sensitive to material type, rather than to the applied stress level. It is apparent that such C-curves cover a wide temperature range, a variety of applied stress levels, and different alloy systems in a single map, so that they can be easily used to develop and design proper working conditions.

The synopsis of this SRC susceptibility study is given here. Motivated by the facts that the roles played by individual contributing factors (including residual stress evolution, microstructural evolution, and detailed failure processes) cannot be quantified and that the hypothesized PFZ-induced localized strains as the SRC driving force have not been experimentally validated, we aim to develop a thermomechanical history in Fig. 2, which provides inputs into a microstructure-explicit, micromechanics-based failure analysis that can quantitatively predict the lifetime with proper governing mechanisms. The weldment experiences a temperature history in Fig. 2(a), where the welding process leads to sharp increase and then decrease of the temperature. Regardless of the subsequent heat treatment or service condition, the reheating is a rapid process, so that it is lumped with welding process for the rateindependent plasticity analysis. This generates the residual stress development in Fig. 2(b). Then the temperature hold at various levels will lead to further stress relaxation, the analysis of which requires a rate-dependent material constitutive law that can be added with cavity damage. This step gives the residual stress evolution in Fig. 2(c). Simultaneously, material microstructures evolve with the formation of PFZ near grain boundaries in Fig. 2(d), the role of which on the lifetime can be analyzed quantitatively in our micromechanical model. The main objectives from these computational studies will be to compare and contrast various contributing factors for SRC, and also to make predictions for susceptibility curves in Fig. 1.

2. Modeling methods

The failure process in austenitic stainless-steel weldments, specifically in 347H steel, is a complex phenomenon influenced by multiple factors that work synergistically. Various types of cracks can be found in weldments (Zhang et al., 2020; Abe et al., 2008), but the most common one is the Type-IV failure with the crack running in the longitudinal

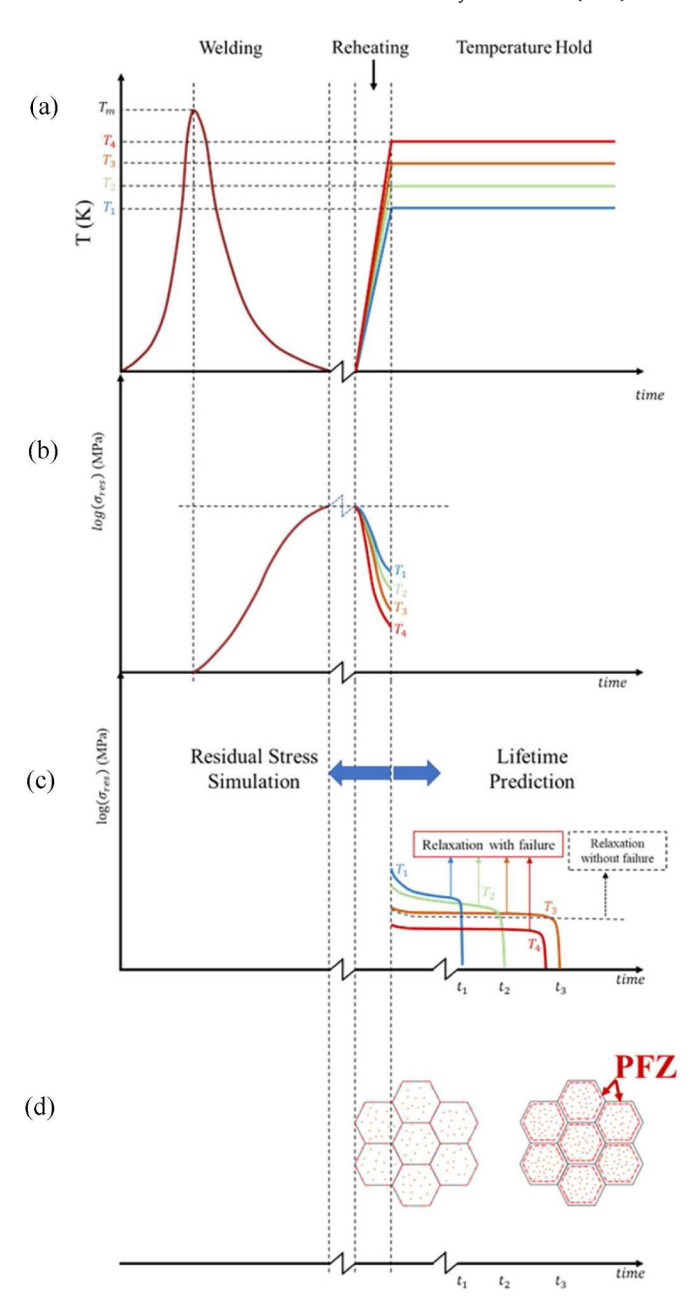


Fig. 2. Schematic illustration of the SRC process: (a) thermal history on the weldment; (b) residual stress generation during welding procedure and its relaxation during reheating process (for PWHT or for service); (c) further residual stress relaxation during temperature hold period (i.e., service condition); (d) microstructural evolution that accompanies with long-time service condition.

direction. Therefore, the two-step simulations as explained in the end of Introduction can be further simplified in Fig. 3. That is, the residual stress analysis in the step of Fig. 2(b) needs to be conducted in a three-dimensional model as shown in Fig. 3(a). Results will be used as the input for the two-dimensional failure model in Fig. 3(b)-3(d), which provides the lifetime results as schematically shown in Fig. 2(c). Our failure model is based on the intergranular cavities, but the microstructures can be anyone from Fig. 3(b)-3(d) and the governing mechanism for cavity growth can be diffusive at low stress and high temperature, or creep-controlled at high stress and intermediate temperature (Gandhi and Ashby, 1979).

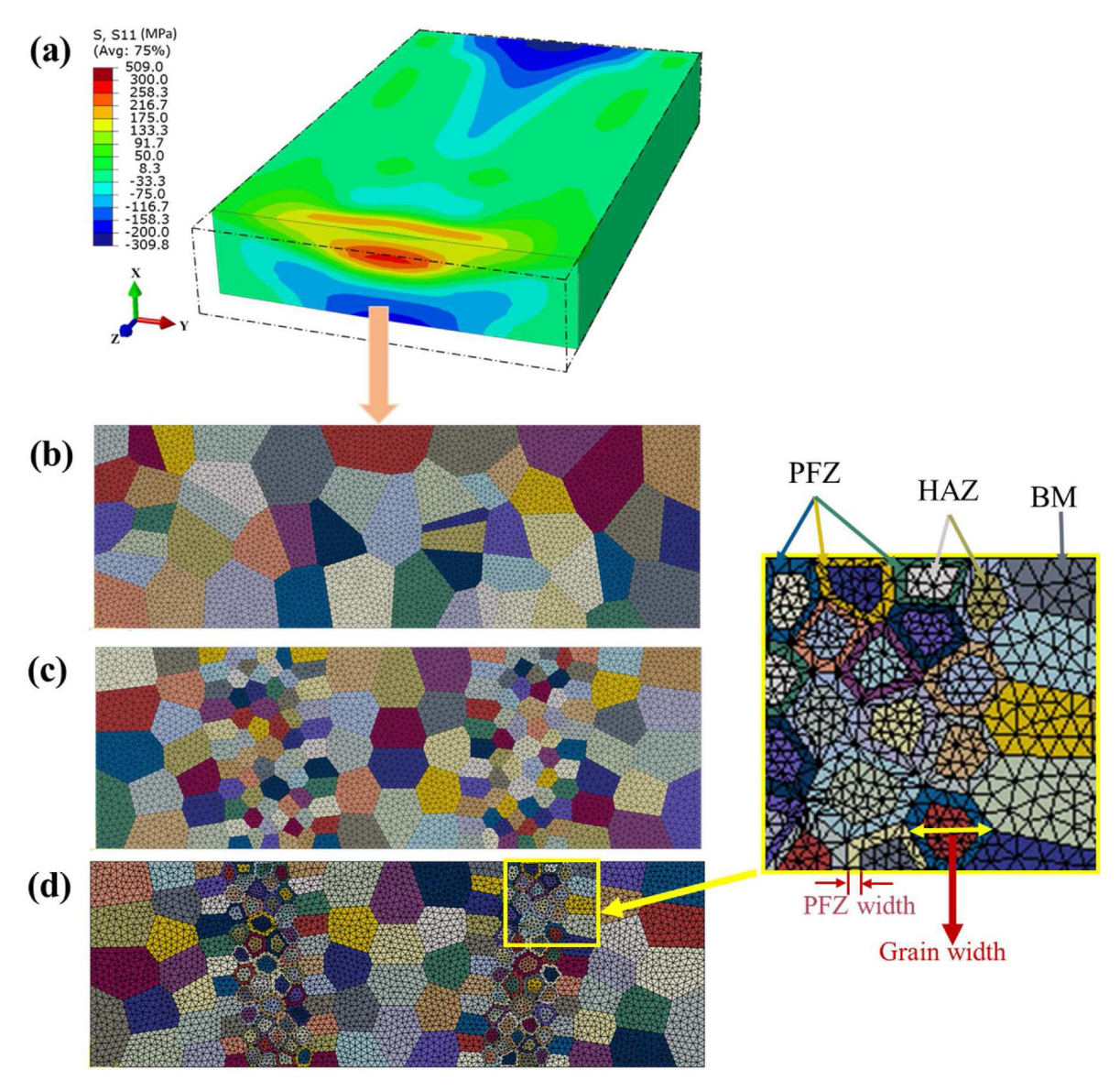


Fig. 3. Overall simulation framework, including the three-dimensional thermomechanical welding analysis in (a), and the corresponding fields passed to the cross-sectional models with (b) ideal microstructure of the base metal, (c) heat affected zone (HAZ), and (d) HAZ with precipitate-free-zone (PFZ) finite element meshes as shown in the inset.

2.1. Residual stress development upon welding and reheating

This is the step pertinent to Figs. 2(b) and Fig. 3(a). We first conduct a heat transfer analysis to determine the temperature distribution, as shown in Fig. 4. It is critical to understand the residual stress in weldments, which is induced by localized and dramatic temperature changes during the welding process. However, accurately capturing the temperature field is challenging due to the difficulty in selecting a heat source model that can precisely describe the melting pool shape. The accuracy of the temperature field distribution is closely related to the heat source model, which affects the temperature gradient in adjacent elements. Therefore, the investigation of melting pool shape is crucial, and previous researchers have conducted studies in this area. Rosenthal (1946) developed a quasi-stationary heat transfer model from the superposition of Green's function of point heat source. It can be seen that a Gaussian-type heat distribution with a prescribed transverse speed mimics the welding process. Further improvements in welding simulations (Goldak et al., 1984; Krutz and Segerlind, 1978) suggest a much appropriate model by adopting a double ellipsoid heat source which is capable of simulating cases lacking radial symmetry. This model can be

easily adjusted for size and shape to match different welding methods, allowing it to simulate both shallow and deep penetration cases. The two ellipsoidal sources can be divided into a front half and a rear half, each corresponding to two different quadrants of an ellipsoid, given by

$$q_f(x,y,z,t) = \frac{6\sqrt{3}f_fQ}{l_{xf}l_{yf}l_{zf}\pi\sqrt{\pi}}e^{-3x^2/l_{xf}^2}e^{-3y^2/l_{yf}^2}e^{-3[z+\nu(\tau-t)]^2/l_{yf}^2}$$
(1)

$$q_r(x, y, z, t) = \frac{6\sqrt{3}f_rQ}{l_{xr}l_{yr}l_{zr}\pi\sqrt{\pi}}e^{-3x^2/l_{xr}^2}e^{-3y^2/l_{yr}^2}e^{-3[x+v(\tau-t)]^2/l_{zr}^2}$$
(2)

where f_f is the fraction of the heat deposited in the front, f_r is the fraction of the heat deposited in the rear, and l_{xf} and others are shape adjusting factors.

Using a reliable heat source model, the temperature field can be generated in the three-dimensional plate model with dimensions of 100 \times 15 \times 60 mm in Fig. 4(a), which is then used to generate the residual stress field. The primary reason for welding to induce residual stress arises from the thermal expansion coefficient mismatch during solidification and cooling between fusion zone (FZ) and surrounding HAZ and

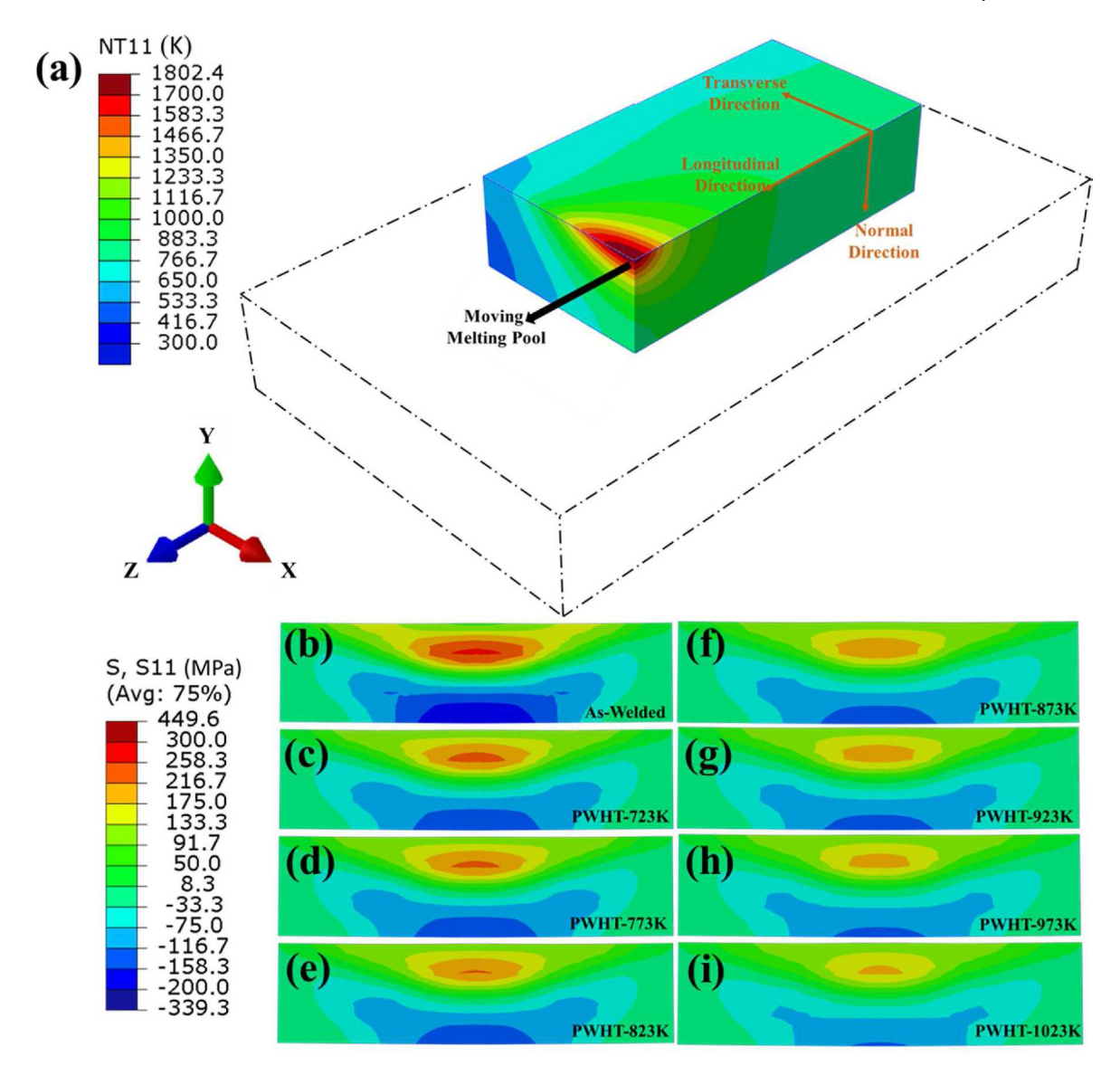


Fig. 4. (a) Three-dimensional simulation model for the welding process, where the heat source moving direction is in the z-axis (longitudinal direction). (b)–(e) Residual stress distribution of model cross-section after welding process and PWHT at 723 K, 773 K, 823 K, 873 K, 923 K, 973 K and 1023 K, respectively.

base metal (BM) materials. Therefore, thermophysical parameters such as latent heat of solidification, specific heat, and others need to be provided, as shown in Table 1(a). Moreover, the residual stress resulting from the above mismatch strain requires the knowledge of thermomechanical parameters such as elastic constants in Table 1(b) and the stress-strain curves at various temperatures in Fig. A1. Following the localized heating and welding step, we then conduct an overall reheating, which is part of the PWHT or service condition. This results into a reduction of residual stress as seen in Fig. 4(b)-4(f), to be explained further in Section 3. Note that simulations in this subsection are for very rapid welding and reheating processes, so that the material constitutive law can be taken as rate-independent in this step.

2.2. Intergranular cavity failure model at elevated temperatures

The failure mechanism observed in this study is Type IV intergranular creep fracture. This type of failure typically occurs in the heat-affected zone (HAZ) at grain boundaries where different length scale precipitations serve as nucleation sites for cavities, as confirmed through microstructure examination. The detailed failure control mechanism and the process of cavity nucleation, cavity growth, and coalescence are

demonstrated as follows.

In this simulation step, rate-dependent inelastic deformation in the grain interior is primarily dominated by dislocation (power-law) creep, while elastic deformation is also involved. Hence, the total strain can be calculated from two separate components, as shown in the equations below:

$$\dot{\varepsilon}_{ij} = \dot{\varepsilon}_{ij}^e + \dot{\varepsilon}_{ij}^p \tag{3}$$

$$\dot{\varepsilon}_{ij}^{e} = \frac{1+v}{E} \left(\dot{\sigma}_{ij} - \frac{v}{1+v} \dot{\sigma}_{kk} \delta_{ij} \right) \tag{4}$$

$$\dot{\varepsilon}_{ij}^{p} = A_{dis} \frac{EbD_{l}}{k_{B}T} \left(\frac{\sigma_{e}}{\sigma_{0}}\right)^{n} \frac{3S_{ij}}{2\sigma_{e}} \overline{M}^{l}$$
(5)

v and E are Poisson's ratio and Young's modulus respectively, δ_{ij} represents the Kronecker delta; k_B is the Boltzmann's constant; b is the Burgers vector; T is the absolute temperature; $\sigma_e = \sqrt{3S_{ij}S_{ij}/2}$ is the von Mises stress; n is the stress exponent; σ_0 is the reference stress; A_{dis} is the material constant; $D_l = D_{l0} \exp\left(-Q_l/RT\right)$ is the diffusivity coefficient for the dislocation creep. And the normalized micromechanical Taylor factor for the I_{th} grain $\overline{M}^l = M^l/max\left(M^1, M^2, \cdots, M^l, \cdots M^N, \right)$, where N is

Table 1(a) Material parameters used for heat transfer analysis. (b) Thermal-mechanical material parameters for residual stress calculation..

(a)	
Thermophysical parameters	
Mass Density (g/mm³)	7.96E-06
Melting Temperature (K)	1719
Latent Heat (J/mol)	40,000
Solidus Temperature (K)	1671
Temperature (K)	Conductivity (W/(mK))
300	0.0134
700	0.0208
1200	0.0335
1600	0.0381
1700	0.0762
Temperature (K)	Specific Heat (J/kg•K)
300	372.2
700	397.3
800	409.8
1200	476.7
1400	493.5

(b)		
Young's Modulus (GPa)	Poisson's Ratio	Temperature (K)
195.1	0.27	294
190.3	0.27	366
186.2	0.29	422
182.7	0.31	477
177.9	0.32	533
174.4	0.31	589
171.0	0.30	644
166.2	0.28	700
162.0	0.26	755
153.1	0.24	866
143.6	0.23	977
131.7	0.22	1089
116.5	0.22	1173
100.0	0.22	1273
80.0	0.22	1373
57.0	0.22	1473
30.0	0.22	1573
2.0	0.22	1673

the total number of grains within the polycrystalline model. \overline{M}^l here is introduced by Raabe et al. (2001) to serve as the slip anisotropy provoked by crystallographic orientation of each grain, which is defined as the ratio of the local accumulated shear $\sum \gamma^{local}$ and local von Mises strain $\langle \varepsilon_{VM}^{local} \rangle$. A separate crystal plasticity finite element simulation needs to be performed, but will not be elaborated here for brevity.

A simplified spherical-cap model is employed to represent the cavities, with a radius of a, half-spacing of b and cavity tip angle $\varphi=75^\circ$ (Onck and van der Giessen, 1997). The cavity volume V and spherical-caps shape parameters h is calculated using following equations:

$$V = \frac{4}{3}\pi a^3 h(\varphi) \tag{6}$$

$$h(\varphi) = \frac{\left[(1 + \cos \varphi)^{-2} - \frac{1}{2} \cos \varphi \right]}{\sin \varphi}$$
 (7)

Due to the difficulty of modeling each individual cavity on the grain boundaries, Rice (1981) proposed a smeared-out representation to simplify the problem. This enables the replacement of discrete distributed cavities with continuous varying separation in the grain boundary. The separation and separation rate equations are listed below:

$$\mu_n = V / (\pi b^2) \tag{8}$$

$$\dot{\mu}_n = \frac{\dot{V}}{\pi b^2} - \frac{2V\dot{b}}{\pi b^3} \tag{9}$$

Based on the pioneering work of Needleman and Rice (1980), the contribution to the volumetric cavity growth rate \dot{V} is decoupled into two parts including the contribution of grain boundary diffusion \dot{V}_1 and the effects of creep deformation \dot{V}_2 which are defined respectively as followed:

$$\dot{V}_{1} = 4\pi D \frac{\sigma_{n} - (1 - f)\sigma_{s}}{\ln\left(\frac{1}{f}\right) - \frac{1}{2}(3 - f)(1 - f)}$$
(10)

$$\dot{V}_{2} = \begin{cases} \pm 2\pi \dot{\varepsilon}_{e}^{c} a^{3} h(\Psi) \left[\alpha_{n} \left| \frac{\sigma_{m}}{\sigma_{e}} \right| + \beta_{n} \right]^{n}, for \left| \frac{\sigma_{m}}{\sigma_{e}} \right| > 1 \\ 2\pi \dot{\varepsilon}_{e}^{c} a^{3} h(\Psi) \left[\alpha_{n} + \beta_{n} \right]^{n} \frac{\sigma_{m}}{\sigma_{e}}, for \left| \frac{\sigma_{m}}{\sigma_{e}} \right| < 1 \end{cases}$$
(11)

Here σ_s represents the sintering stress, $\alpha_n=3/(2n)$ and $\beta_n=(n-1)(n+0.4319)/n^2$, and f is the effective cavity volume fraction given by

$$f = max \left[\left(\frac{a}{b} \right)^2, \left(\frac{a}{a+1.5L} \right)^2 \right]$$
 (12)

In this equation, L is a material length scale dependent on stress and temperature able to demonstrate the combination of diffusion and creep deformation to the cavity growth (Rice, 1979) which can described as follow:

$$L = \left[D \frac{\sigma_e}{\dot{\varepsilon}_e^c} \right]^{1/3} \tag{13}$$

When L is much larger than a, the effect of creep deformation became trivial. In comparison, the impact of grain boundary diffusion on the cavity growth is decreasing as L turns smaller. In the above equation, D is the grain boundary diffusion parameters defined as follows:

$$D = \frac{D_{b0}\delta_b\Omega}{k_BT}\exp\left(\frac{-Q_b}{RT}\right)$$
 (14)

where Q_b is the activation energy in grain boundary diffusion, $D_{b0}\delta_b$ is the grain boundary diffusion coefficient, Ω is the atom volume. Hence, the cavity growth rate can be derived as

$$\dot{a} = V/(4\pi a^2 h(\Psi)) \tag{15}$$

As one of the competing mechanisms on creep deformation and damage of ferritic steel weldments (Abe et al., 2008; Kimmins and Smith, 1984), grain boundary sliding behaves in a Newtonian viscous manner (Ashby, 1972) and is essentially a thermally activated process, governed by

$$\dot{\mu}_{t} = \frac{\Omega \eta_{0} \exp\left(-Q_{gbs}/RT\right)}{k_{B}T} \sigma_{t} \tag{16}$$

Here $\dot{\mu}_t$ is the relative sliding velocity of adjoining grains initiated by the shear stress σ_t in the grain boundary, η_0 is a characteristic sliding velocity, Q_{gbs} is the activation energy for the grain boundary sliding.

Based on the constitutive law outlined above, Zhang et al. (2020) proposed a nonlinear finite element method that connects directly to the material microstructure. Specifically, the elastic deformation and dislocation creep in the grain interior were defined using a user-defined material (UMAT) subroutine implemented in ABAQUS. Meanwhile, the grain boundary cavitation and grain boundary sliding (GBS) were modeled using a rate-dependent cohesive element through a user-defined element (UEL) subroutine. Building upon their previous work, a two-dimensional digital model containing microstructure features was created to compare various microstructure settings with the

actual microstructure evolution. Three different cases were simulated by gradually adding microstructure features, beginning with only the base metal case. This allowed the simulation results to be fitted to available experimental data (e.g., those from National Institute of Materials Science (NIMS), Japan). Subsequently, the fusion zone and HAZ were included to decrease the gap between the simulation model and actual morphology, due to the magnitudes of thermal-mechanical properties differing among the BM, HZA, and FZ.

Finally, the precipitation free zone (PFZ) was incorporated into the model, which is related to the microstructure feature of the late service stage of the service component. Precipitation concentration leads to strengthening of the grain interior, while the dissipation of particles at grain boundaries results in the formation of PFZ and weakening of grain boundaries. This behavior plays a crucial role in the initiation and propagation of cracks during the late service stage. To simulate these cases, digital microstructures were established separately with random crystallographic orientations and material properties assigned through UMAT subroutine, as illustrated in Fig. 3(d). The boundary conditions of the simulation model were established to compare with the actual service situation, with fixed left and right edges and free expansion at the bottom and top surfaces. By choosing different ratios between PFZ thickness and grain size, we are able to examine the role of microstructural evolution on the SRC susceptibility.

3. Results

3.1. Residual stress history in Fig. 2(b)

By employing the double ellipsoidal heat source model, the temperature and melting pool shape can be replicated with high fidelity compared to real welding processes. The temperature field obtained through this method can then be used to generate the residual stress field after the welding procedure and after exposure to different reheating temperatures. The thermal-mechanical properties, failure mechanisms, and microstructure are highly dependent on temperature and stress field variation. Therefore, it is important to determine the distribution of the residual stress field and the influence brought by reheating temperatures. A cross-section located at the midpoint of the three-dimensional plate was selected to extract the residual stress field, perpendicular to the longitudinal direction which is also the heat-source moving direction. A quarter section of the 3D model is shown in Fig. 4(a) to demonstrate the melting pool and the relationship of each direction. Fig. 4(b)-(i) show the residual stress field under different thermal treatments, with (b) as the after-welding case, and reheating temperatures ranging from 723 K to 1023 K in 50 K intervals. The residual stress values can be read from the legend color bar. As the reheating temperature increases, the residual stress gradually decreases from the highest value of 450 MPa in the after-welding case to ~160 MPa in the case exposed to reheating to 1023 K. The highest compressive residual stress is found in the after-welding case at -340 MPa. The residual stress reduction percentage in each simulated temperature can be calculated, using the following equations:

$$\frac{\Delta T}{T} = \frac{T_{PWHT} - RT}{T_{PWHT}} \tag{17}$$

$$\sigma_{reduction} = \frac{-(\sigma_{PWHT} - \sigma_{As-welded})}{\sigma_{As-welded}}$$
(18)

As shown by the results in Fig. 5, the fitted curve indicates a linear relationship, suggesting that as the reheating temperature increases, the residual stress reduction percentage increases accordingly. A slope can be obtained from the fitting results, and the residual stress reduction percentage at other temperature variation rates can be predicted approximately. The reason for such a residual stress reduction is again from thermal expansion coefficient mismatch. The prediction on the residual stress field distribution for both welding process and different

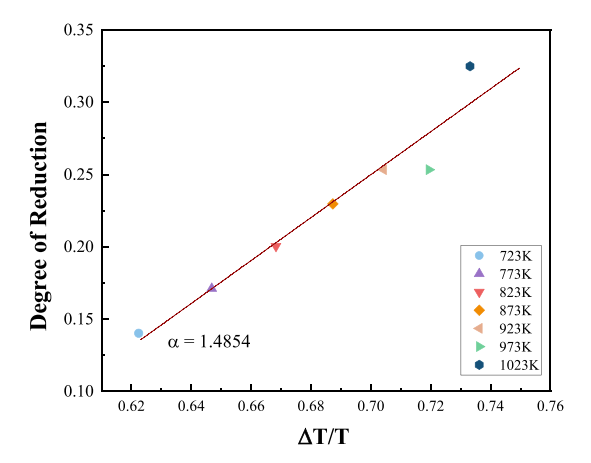


Fig. 5. The residual stress reduction in Fig. 4(b)-4(e) is found to obey a linear relationship to the reheating temperature.

PWHT procedure were calculated based on this.

The 2D failure model aims to simulate the failure process of components at the temperature hold stage in Fig. 2(c). To achieve this, the microstructure setup needs to combine the residual stress field to perform the prediction. The three different microstructure setups have varying grain sizes and distributions. Previous research has shown that HAZ accumulates the highest residual stress under various working conditions. Therefore, in the 2D failure model, it is crucial to ensure that the highest residual stress is located in the HAZ. During welding, the weld zone is typically in a V-shape or X-shape to avoid bending or warpage behavior, which can cause further stress concentrations. Consequently, the FZ and HAZ are not perfectly perpendicular to the plate top and bottom surface, and a specific angle of approximately 50°-70° is usually applied to flatten the weldments. While results in Fig. 4 are for a single-pass welding procedure, the temperature and residual stress fields and their evolution in a multiple-pass procedure are qualitatively similar. Particularly, the residual stress field is concentrated on the HAZs. For brevity, we will not present the simulation details, but use the following simplified residual stress field. A usersubroutine-defined initial stress field (SIGINI) is introduced using the following equation:

$$\sigma_r = y_0 + \frac{A}{\left(w \times \sqrt{\frac{\pi}{4 \times \ln(2)}}\right)} \times exp\left(-4 \times \ln(2) \times (x - x_c)^2 / w^2\right)$$
 (20)

where y_0 , A, w and x_c are set as 50 MPa, 500 MPa, 10.4 mm and 14.1 mm respectively, as obtained from fitting to results in Fig. 4(b). For other cases, the fitted parameters will change accordingly, but they will not be tabulated here for brevity.

3.2. Lifetime prediction in Fig. 2(c)

The reliability of lifetime prediction in different microstructures is based on the accuracy of base metal material parameters used in simulation model. Before deducing the material parameters for HAZ, it is necessary to compare the simulation results with creep test results on the base metal. Fig. 6 shows the results of the creep test for base metal at four different temperature levels, which have been fit well by adjusting several main control factors and considering other factors as shown in Table 2. However, due to the limited creep data available for 347H stainless steels in the NIMS database, it is necessary to extrapolate the results for other temperatures using the creep and Arrhenius equations. The main influence factors, such as stress exponent n, cavity nucleation

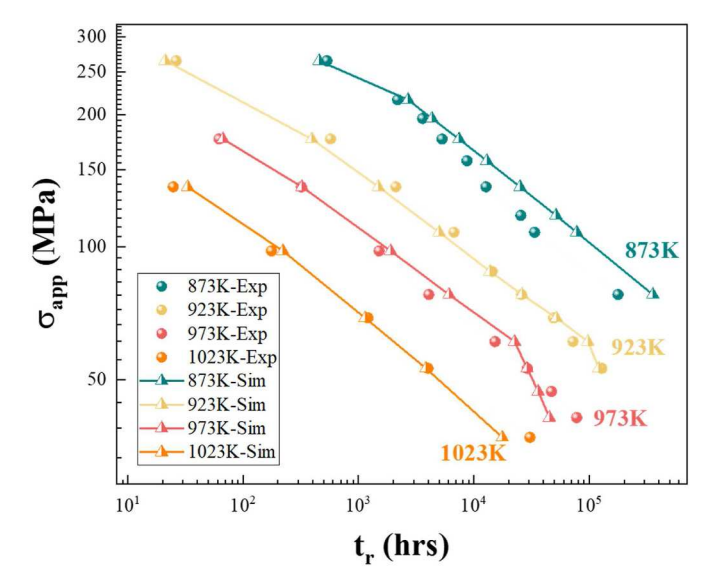


Fig. 6. Experimental creep test data of 347 stainless steel from National Institute of Materials Science (NIMS), Japan, at 873 K, 923 K, 973 K and 1023 K under different applied loads. Simulation results are based on the intergranular cavity model.

 Table 2

 Representative values for material parameters in base metal (BM) at different temperatures.

Parameter	873 K	923 K	973 K	1023 K
Reference stress (MPa)	142	142	142	142
Stress exponent, n	6.25	7.65	8.32	5.44
Grain size (10^{-3}mm^{-3})	5	5	5	5
Cavity nucleation parameter (10^{-8})	1.5	6	6	6
Heterogeneity factor	1	1	1	1
Reference stress for nucleation law (MPa)	100	100	100	100
Poisson's ratio, ν	0.3	0.3	0.3	0.3
Young's modulus, E (GPa)	146.6	142.0	137.3	132.6
Diffusion parameter, D	1.10×10^{-21}	5.33×10^{-21}	2.19×10^{-20}	5×10^{-20}
Grain boundary viscosity	$\begin{array}{c} 5.81 \times \\ 10^{14} \end{array}$	1.20×10^{14}	$\begin{array}{c} 2.93 \times \\ 10^{13} \end{array}$	$\begin{array}{c} 8.2 \times \\ 10^{12} \end{array}$
Reference strain rate	1.416×10^{-9}	1.159×10^{-8}	6.099×10^{-8}	1.405×10^{-6}

parameter F_n , grain boundary diffusivity D, grain boundary viscosity etc., were determined using the Arrhenius equation $\ln k = \ln A + \frac{-E_a}{RT}$, (k is rate constant, A is frequency factor, E_a is activation energy, R is gas constant, T is temperature in Kelvin) and the formatted creep rate relation with applied stress through a power law. The comparison between the experimental discrete data and the simulation line connected data shows a good correlation between them. The experimental data also revealed two different slopes, which correspond to creep and diffusion failure mechanisms. The slope change occurs at a low stress level, as the lifetime reach 10,000 h, especially for 973 K case. The slope of experimental discrete data for $\log(\sigma) - \log(t_r)$ is approximately equal to -1, which indicates the lifetime is inversely proportional to the stress. This agrees with the conclusion of Hull and Rimmer (1959) that creep failure is purely controlled by atom diffusion type-induced cavity growth under low applied stress. As the applied stress decreases, the rupture time increases, and a no failure case will occur when the residual stress decreases to a critical value that is not available in real experiments.

Experimental data for the HAZ and FZ, which govern the lifetime of service components, are rarely available. Therefore, an estimation can

be made to generate material parameters for the FZ and HAZ if considering one order of magnitude shorter lifetimes in these locations than in BM, which is suggested from limited weldment failure data (Zhang et al., 2020). The corresponding HAZ constitutive parameters are given in Table 3. The presence of PFZ removes the strengthening precipitates so that the creep resistance is reduced. Again there is a lack of quantitative measurements, but the literature studies (Unwin et al., 1969; Jiang and Faulkner, 1996; Ryum, 1968) suggest one order of magnitude increase of the strain rate for the dislocation creep in Eq. (5).

Three microstructural setups in Fig. 3 are simulated to obtain the stress versus time plots in Fig. 7, where the stress should be interpreted as the overall magnitude of the stress fields, at the hold temperatures of 873 K and 1023 K in (a) and (b), respectively. Without the cavity failure model, the residual stress relaxation will continue slowly to infinite time. Adding cavities and also considering more realistic microstructures, the stress-time curves show sudden drops that correspond to the coalescence of grain boundary cavities, from which the lifetimes can be determined. For example, at 873 K, the BM-only case has a failure time of 1.353×10^9 hours, which decreases to 3.332×10^8 hours in the HAZ case, and further reduces to 1.682×10^8 hours in the HAZ + PFZ case. At 1023 K, the corresponding lifetimes are 4.514×10^7 , 3.541×10^6 , and 6.889×10^5 hours, respectively. The comparison of the four microstructure cases indicates that the microstructure gradient is responsible for shortening the failure time. Despite the enhancement of mechanical properties through precipitation strengthening particle formation (NbC), the degrading impact caused by the widening of PFZ becomes more pronounced with increasing service time. The competitive relationship between these two factors is time-dependent and influenced by the service temperature. As NbC migrates into the grain interior and the volume fraction of PFZ increases, the thermal-mechanical properties difference on the grain boundary enlarges. The contribution of other types of precipitations (e.g., M23C6, G-phase, Z-phase etc., which preferentially formed at GB) accelerates the voids formation, coalescence, and crack propagation process.

3.3. Susceptibility C-curves

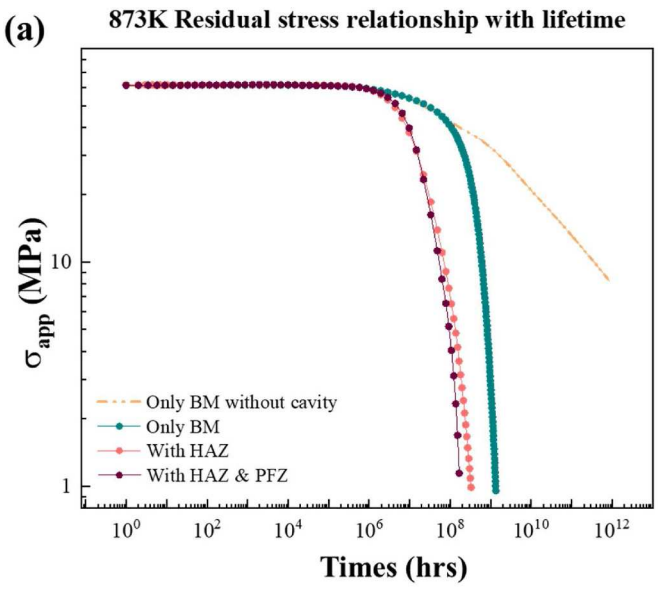
Besides the two examples in Fig. 7, we can now generate a full set of susceptibility curves as those in Fig. 1, by applying various residual stress levels at different temperatures onto the microstructures in Fig. 3. Based on results in Fig. 5, we can apply a residual stress field according to the following

$$\sigma_{res}^{magnitude}\left(T_{reheating}\right) = \sigma_{res}^{magnitude}\left(T_{ref}\right) \times \left(1 - \alpha \frac{T_{reheating} - T_{ref}}{T_{ref}}\right) \tag{19}$$

where T_{ref} is the reference temperature (room temperature here),

Table 3Representative values for material parameters in heat affected zone (HAZ) at different temperatures.

Parameter	873 K	923 K	973 K	1023 K
Reference stress	0.142 GPa	0.142 GPa	0.142 GPa	0.142 GPa
Stress exponent, n	6.25	7.65	8.32	5.44
Grain size	5 ×	5 ×	5 ×	5 ×
	10^{-3} mm	10^{-3} mm	10^{-3} mm	10^{-3} mm
Cavity nucleation parameter	5×10^8	1.7×10^9	2.6×10^9	3.2×10^9
Heterogeneity factor	1	1	1	1
Reference stress for nucleation law	0.100 GPa	0.100 GPa	0.100 GPa	0.100 GPa
Poisson's ratio, ν	0.3	0.3	0.3	0.3
Diffusion parameter, D	4×10^{-20}	1.94 ×	7.96 ×	$1.82 \times$
		10^{-19}	10^{-19}	10^{-18}
Grain boundary	5.81 ×	$1.20 \times$	2.93 ×	8.2×10^{11}
viscosity	10^{13}	10^{13}	10^{12}	
Reference strain rate	1.416 ×	$1.159 \times$	6.099 ×	1.405 \times
	10^{-8}	10^{-7}	10^{-7}	10^{-5}



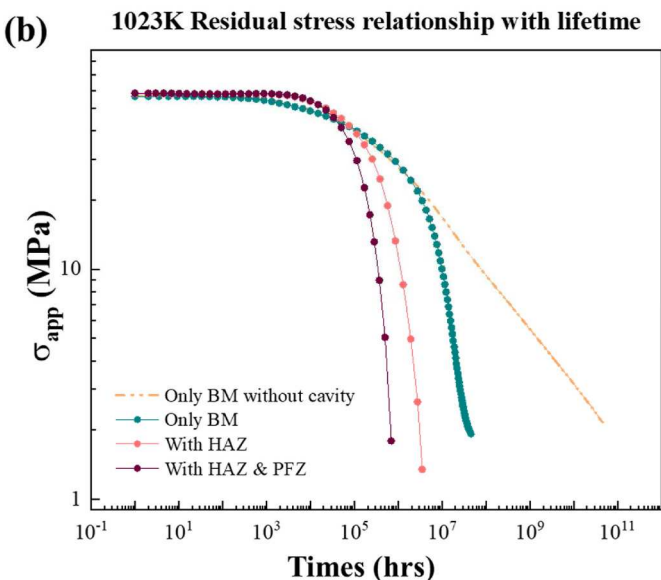


Fig. 7. Residual stress variation in simulation models with different microstructures: only base metal without cavity failure; only base metal with cavity failure model; weldment with HAZ failure; weldment with HAZ and PFZ. Refer to Fig. 3 for these microstructures. These stress relaxation history results can be compared to the schematic illustration in Fig. 2(c). (a) 873 K and (b) 1023 K.

 $T_{reheating}$ is gradually increasing from 873 K to 1023 K with a 50 K interval, and α is the parameter reflecting the reduction rate of residual stress and it can be adjusted in a range.

Results in Fig. 8 show the susceptibility C-curves for 347H stainless steels with the three microstructural setups in Fig. 3. The residual stress level is obtained from Eq. (19) with various α (using 0.1 and 0.4 here as representative values), and the temperature spans a range that sees the transition of cavity growth mechanisms. As expected, the base-metal case with a higher α value corresponds to a longer lifetime under the same working conditions, and gives a clear C-shape here. An elevated residual stress and a microstructure with degraded HAZ and/or PFZ will reduce the lifetime significantly, by two or three orders of magnitude in this plot. The ratio between the PFZ width (see Fig. 3) and the average HAZ grain size is defined as β , chosen as 1/2 and 1/5 in the last two examples in Fig. 8. A larger value of this ratio indicates that the region without precipitation is larger, so that the grain interior is less creepresistant. The PFZ width of 1/2 gives the shortest lifetime among

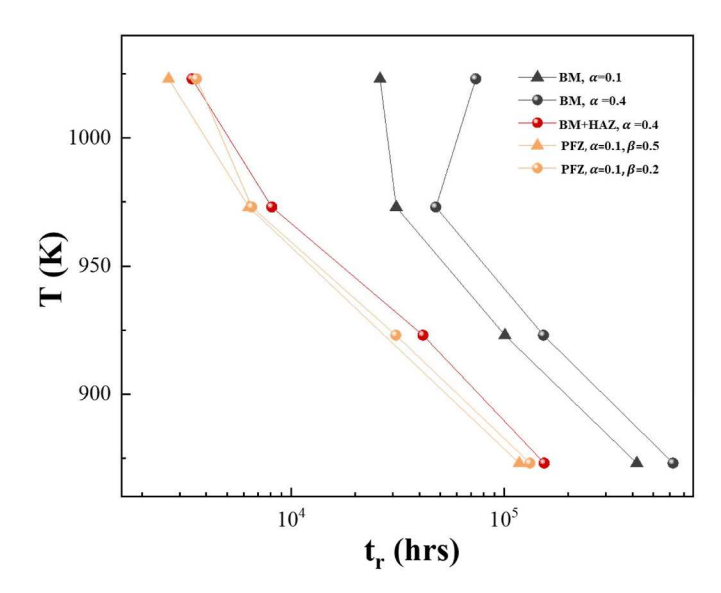


Fig. 8. Relationship between lifetime and reheating-and-hold temperature under different microstructures (similar to the cases in Fig. 7). The thickness ratio of PFZ layer to grain size in the HAZ is taken to be $\beta=1/2$ and 1/5 for comparison purpose.

these five conditions, which can be considered the upper limit of the PFZ width. These predictions compare qualitatively well with available experiments in Fig. 1. However, many experiments have an applied stress which significantly shorten the lifetime. For example, from NIMS data in Fig. 6, we can easily see that a lifetime of about 10^4 h at 973 K can be easily reduced to 10^2 h with an addition of 100 MPa external load, or to 10° h with 300 MPa. Thus, they agree favorably with Fig. 1. It should be emphasized again that due to the microstructural heterogeneities in this problem, it is not possible to get the local constitutive parameters at HAZ and PFZ. Nevertheless, the estimated parameters in Tables 2 and 3 still lead to reasonable predictions, especially the formation of C-shaped curves.

From all the above simulation results, we can now quantitatively compare the roles played by individual contributing factors for SRC. As shown in Fig. 9, the residual stress evolves significantly during welding (mainly due to the thermal expansion mismatch during solidification and among FZ, HAZ and BM) and during overall reheating (primarily caused by the reduced degree of thermal expansion mismatch). In the temperature-hold stage, there is a very slow stress relaxation process due to the creep deformation of the material. Simultaneously, grain boundary cavities grow and coalescence, microstructures evolve, and eventually a lifetime is reached with a corresponding sudden load drop. There are several possible scenarios from the synergy of these factors.

- Residual stress history is the primary factor that controls the SRC susceptibility.
- If the stress relaxation is significant in the reheating stage (i.e., a large α from Fig. 5), the SRC susceptibility curve will easily be C-shaped. That is, at very high temperature, the lifetime is more extended due to a much reduced residual stress upon reheating.
- Realistic calculations show the lifetimes on the order of years, which
 correspond to diffusive cavity growth. Laboratory experiments that
 mimic SRC are often employed with additional loading, thus leading
 to the change of governing mechanism to grain-interior-creep
 controlled cavity growth on the grain boundaries.
- The presence of PFZ (i.e., as indicated by β in Figs. 3 and 8) will further reduce the lifetime significantly, due to the low creep resistance thereof. The increase in the creep strain rate will accelerate the cavity growth as shown in Eq. (11).

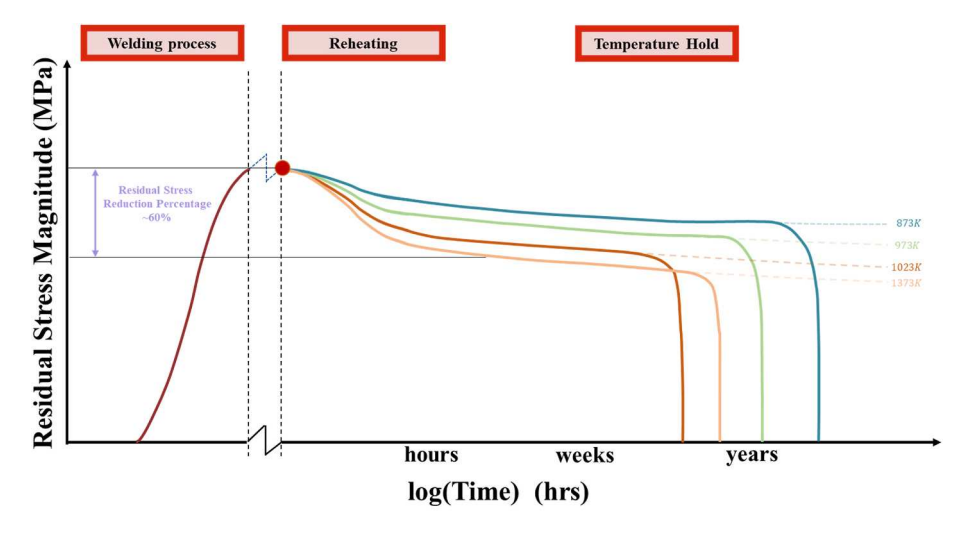


Fig. 9. Schematic drawing of the residual stress evolution, where light dotted lines show the residual stress variation trend for the case without cavity failure, thick solid lines are with cavities, and thick dashed lines with cavity failure and PFZ added to the HAZ grains.

Furthermore, we can describe the roles of α and temperature-dependent material strength on the SRC susceptibility plot, as shown in Fig. 10. A higher α corresponds to a lower residual stress level upon reheating, which can guarantee a longer lifetime. Since this parameter is more sensitive to thermophysical and thermomechanical parameters, it is thus imperative to examine other materials or filler materials to validate this prediction. The yield stress drop with respect to the temperature increase, $\frac{\partial \sigma_{YS}}{\partial T}$, also controls the level of residual stress upon reheating. A higher value of $\left|\frac{\partial \sigma_{YS}}{\partial T}\right|$ within the same temperature range indicates a faster drop in yield strength, leading to a lower susceptibility to crack formation. The schematic drawings in Fig. 10, with $\alpha_1 > \alpha_2 > \alpha_3$ and $\left|\frac{\partial \sigma_{YS}}{\partial T}\right|_2 > \left|\frac{\partial \sigma_{YS}}{\partial T}\right|_3$, describe these parameters and thus can be used for guidance of material design and safety analysis.

4. Conclusions

Identifying the controlling failure mechanisms and performing lifetime predictions consistently remain a difficulty for weldments subjected to various heat treatments. It is known that residual stress evolution, microstructural change, and detailed failure processes that distribute stress and strain concentrations all contribute to the final SRC and SAC, but a quantitative assessment of these synergistic factors is not feasible experimentally. In this work, focusing on the SRC susceptibility of 347H stainless steel weldments, we develop two simulation steps, the

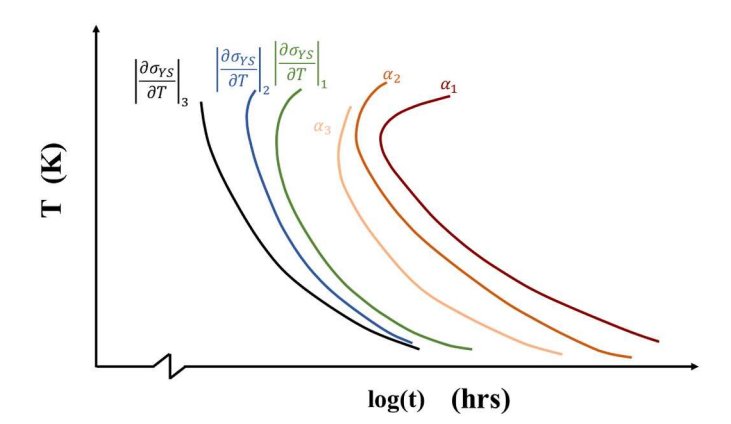


Fig. 10. Schematic illustration of the shifting of C-curves under different residual stress reduction rate (α_1 being the highest; see Fig. 5) and different strength-temperature dependence ($|\frac{\partial \sigma_{\text{TS}}}{\partial T}|_1$ being the highest; see Fig. A1(b)).

first one on the residual stress development during welding and upon reheating, and the second on the microstructure-explicit, micromechanics-based failure processes. Despite the limited knowledge of material constitutive parameters in the heterogeneous microstructure, it is found that the leading factor is the residual stress development, reduction and evolution, while others (especially the PFZ) at most change the lifetime's order of magnitude but not its trends. The SRC susceptibility C-curves can be reproduced in some cases, and comparisons with literature experiments are made when considering additional applied load. Further comparisons to nondestructive and in situ residual stress measurements are eagerly awaited.

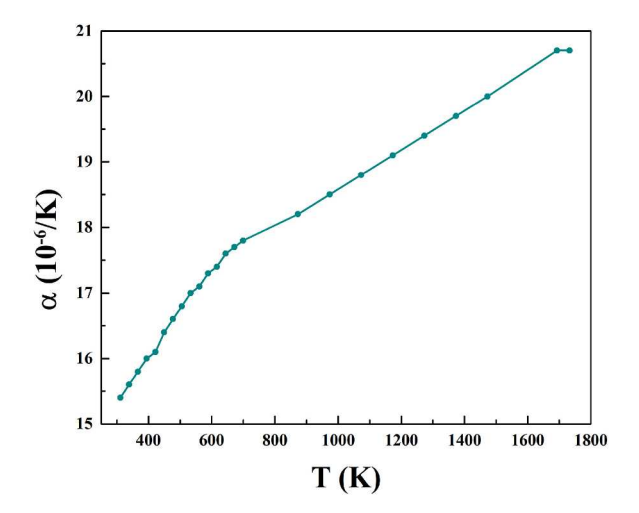
CRediT authorship contribution statement

Yi Yang: Conceptualization, Data curation, Formal analysis, Funding acquisition, Investigation, Methodology, Resources, Software, Validation, Visualization, Writing - original draft, Writing - review & editing. Dong Han: Conceptualization, Data curation, Formal analysis, Investigation, Methodology, Project administration, Resources, Software, Validation, Visualization, Writing – original draft, Writing – review & editing. Wei Zhang: Conceptualization, Data curation, Formal analysis, Investigation, Methodology, Project administration, Resources, Software, Supervision, Validation, Visualization, Writing - original draft, Writing - review & editing. Yanfei Gao: Conceptualization, Data curation, Formal analysis, Funding acquisition, Investigation, Methodology, Project administration, Resources, Software, Supervision, Validation, Visualization, Writing - original draft, Writing - review & editing. Jorge Penso: Conceptualization, Data curation, Formal analysis, Funding acquisition, Investigation, Methodology, Project administration, Resources, Software, Supervision, Validation, Visualization, Writing - original draft, Writing - review & editing. Zhili Feng: Conceptualization, Data curation, Formal analysis, Funding acquisition, Investigation, Methodology, Project administration, Resources, Software, Supervision, Validation, Visualization, Writing - original draft, Writing – review & editing.

Declaration of competing interest

The authors declare that they have no known competing financial interests or personal relationships that could have appeared to influence the work reported in this work.

(a)



294K 800 -693K 923K 1089K 1366K 600 1550K $\sigma_{\rm Y}$ (MPa) 200 0 0.2 0.8 0.0 0.4 0.6 $\varepsilon_{\rm p}$

Fig. A1. Material properties used for the residual stress calculations: (a) thermal expansion coefficient, and (b) stress versus plastic strain curves at various temperatures.

Data availability

(b)

Data will be made available on request.

Acknowledgements

The authors would like to acknowledge the financial support of Shell Global Solutions, made possible through IIP-1540000, IIP-1822186, and IIP-2052729 from the US National Science Foundation, Industry University Cooperative Research Center (I/UCRC) program, to the University of Tennessee under the Manufacturing and Materials Joining Innovation Center (Ma2JIC). YY also acknowledges the GATE Fellowship from the University of Tennessee. YG is grateful to fruitful discussions with Prof. Zhenzhen Yu at Colorado School of Mines. This work belongs to the Materials Mechanics Beyond the Horizon – The Alan Needleman 80th Anniversary Issue.

Appendix A

In the residual stress analysis of Section 2.1, thermophysical properties such as the thermal expansion coefficient and thermomechanical properties such as the stress-strain curves at elevated temperatures are

needed. They are given in Figs. A1(a) and A1(b), respectively.

References

Abe, F., Kern, T.U., Viswanathan, R., 2008. Creep-Resistant Steels. Woodhead Publishing. Ashby, M.F., 1972. Boundary defects, and atomistic aspects of boundary sliding and diffusional creep. Surf. Sci. 31, 498–542.

Bauer, C.L., Lessmann, G.G., 1976. Metal-joining methods. Annu. Rev. Mater. Sci. 6, 361–387

Chang, J.C., Kim, B.S., Heo, N.H., 2011. Stress relief cracking on the weld of T/P 23 steel. Procedia Eng. 10, 734–739.

Dong, P., Song, S., Zhao, J., 2014. Analysis of residual stress relief mechanisms in postweld heat treatment. Int. J. Pres. Ves. Pip. 122, 6–14.

Gaffard, V., Gourgues-Lorenzon, A.F., Besson, J., 2005. High temperature creep flow and damage properties of 9Cr1MoNbV steels: base metal and weldment. Nucl. Eng. Des. 235, 2547–2562.

Gandhi, C., Ashby, M.F., 1979. Overview no. 5: fracture-mechanism maps for materials which cleave: FCC, BCC and HCP metals and ceramics. Acta Metall. 27, 1565–1602.

Goldak, J., Chakravarti, A., Bibby, M., 1984. A new finite element model for welding heat sources. Metall. Trans. A B 15, 299–305.

Hayhurst, D.R., Goodall, I.W., Hayhurst, R.J., Dean, D.W., 2005. Lifetime predictions for high-temperature low-alloy ferritic steel weldments. J. Strain Anal. 40, 675–701.

Hull, D., Rimmer, D.E., 1959. The growth of grain-boundary voids under stress. Phil. Mag. 4, 673–687.

Jiang, H., Faulkner, R.G., 1996. Modelling of grain boundary segregation, precipitation and precipitate-free zones of high strength aluminium alloys—I. The model. Acta Mater. 44, 1857–1864.

Kim, Y.S., Ahn, S.B., Cheong, Y.M., 2007. Precipitation of crack tip hydrides in zirconium alloys. J. Alloys Compd. 429, 221–226.

Kimmins, S., Smith, D., 1984. On the relaxation of interface stresses during creep of ferritic steel weldments. J. Mech. Phys. Solid. 32, 373–393.

Kromm, A., Lausch, T., Schroepfer, D., Rhode, M., Kannengiesser, T., 2020. Influence of welding stresses on relief cracking during heat treatment of a creep-resistant 13CrMoV steel Part II: mechanisms of stress relief cracking during post weld heat treatment. Weld. World 64, 819–829.

Krutz, G.W., Segerlind, L.J., 1978. Finite element analysis of welded structures. Welding Research Supplement 211–216.

Mahajanam, S.P.V., Joosten, M.W., 2011. Guidelines for filler-material selection to minimize preferential weld corrosion in pipeline steels. SPE Proj. Facil. Constr. 5–12.
 Nawrocki, J.G., Dupont, J.N., Robino, C.V., Marder, A.R., 1999. The stress-relief cracking susceptibility of a new ferritic-steel Part I: single-pass heat-affected zone simulations.

Welding Journal Research Supplement 1–21.
Nawrocki, J.G., Dupont, J.N., Robino, C.V., Puskar, J.D., Marder, A.R., 2003. The mechanism of stress-relief cracking in ferritic alloy steel. Supplement to The Welding Journal 25–35.

Needleman, A., Rice, J.R., 1980. Plastic creep flow effects in the diffusive cavitation of grain boundaries. Acta Metall. 28, 1315–1332.

Onck, P., van der Giessen, E., 1997. Microstructurally-based modelling of intergranular creep fracture using grain elements. Mech. Mater. 26, 109–126.

Pulliam, G.R., 1959. Precipitation in microscopic cracks. J. Am. Ceram. Soc. 42, 477–482.

Raabe, D., Sachtleber, M., Zhao, Z., Roters, F., Zaefferer, S., 2001. Micromechanical and macromechanical effects in grain scale polycrystal plasticity experimentation and simulation. Acta Mater. 49, 3433–3441.

Rice, J.R., 1979. Time Dependent Fracture of Materials at Elevated Temperature. US Department of Energy Report, pp. 130–145.

Rice, J.R., 1981. Constraints on the diffusive cavitation of isolated grain boundary facets in creeping polycrystals. Acta Metall. 29, 675–681.

Rosenthal, D., 1946. The theory of moving sources of heat and its application to metal treatments. Transactions of the ASME 68, 849–865.

Rossini, N.S., Dassisti, M., Benyounis, K.Y., Olabi, A.G., 2012. Methods of measuring residual stresses in components. Mater. Des. 35, 572–588.

Ryum, N., 1968. The influence of a precipitate-free zone on the mechanical properties of an Al-Mg-Zn alloy. Acta Metall. 16, 327–332.

Sarich, C., Alexandrov, B., Benatar, A., Penso, J., 2022. Test for stress relief cracking susceptibility in creep resistant chromium-molybdenum steels. Sci. Technol. Weld. Join. 4, 265–281.

Shin, J., McMahon Jr., C.J., 1984. Mechanisms of stress relief cracking in a ferritic steel. Acta Metall. 32, 1535–1552.

Siefert, J.A., Shingledecker, J.P., DuPont, J.N., David, S.A., 2016. Weldability and weld performance of candidate nickel based superalloys for advanced ultrasupercritical fossil power plants Part II: weldability and cross-weld creep performance. Sci. Technol. Weld. Join. 21, 396–428.

Unwin, P.N.T., Lorimer, G.W., Nicholson, R.B., 1969. The origin of the grain boundary precipitate free zone. Acta Metall. 17, 1363–1377.

Wu, Z., Penso, J., Chen, T., Leonard, D.N., Zhang, D., David, S.A., Feng, Z., 2020. Microstructural examination of 347H austenitic stainless steel weld after 30-years' refinery service. Proceedings of the ASME Pressure Vessels & Piping Conference, pp. PVP2020–21641.

Zhang, W., Wang, X., Wang, Y., Yu, X., Gao, Y., Feng, Z., 2020. Type IV failure in weldment of creep resistant ferritic alloys: II. Creep fracture and lifetime prediction. J. Mech. Phys. Solid. 134, 103775.